Pattern Recognition 43 (2010) 3522–3538

Contents lists available at ScienceDirect

Pattern Recognition

journal homepage: www.elsevier.com/locate/pr

# Continuous force field analysis for generalized gradient vector flow field

Annupan Rodtook [a], Stanislav S. Makhanov [b,*]

[a] Department of Computer Science, Ramkhamhaeng University, Bangkok 10240, Thailand
[b] School of Information, Computer and Communication Technology, Sirindhorn International Institute of Technology, Thammasat University, Thailand

ARTICLE INFO

*Article history:*
Received 6 October 2008
Received in revised form
10 January 2010
Accepted 6 April 2010

*Keywords:*
Gradient vector flow
Snakes
Segmentation
Ultrasound image
Breast tumor

ABSTRACT

We propose a modification of the generalized gradient vector flow field techniques based on a continuous force field analysis. At every iteration the generalized gradient vector flow method obtains a new, improved vector field. However, the numerical procedure always employs the original image to calculate the gradients used in the source term. The basic idea developed in this paper is to use the resulting vector field to obtain an improved edge map and use it to calculate a new gradient based source term. The improved edge map is evaluated by new continuous force field analysis techniques inspired by a preceding discrete version. The approach leads to a better convergence and better segmentation accuracy as compared to several conventional gradient vector flow type methods.



## 1. Introduction

Among the most promising techniques for extraction of complex objects from digital images are active contours or snakes, originally introduced by Kass et al. [1]. Since the seminal work of Kass and colleagues, techniques based on active contours have been applied to many object extraction tasks.

In particular, the snakes have been used to locate the object boundaries in various applications of medical image processing with a different degree of success. In particular, they have been successfully applied to segmentation of dangerous tumors in the images of the human heart, liver, brain, breast, etc. [2–12].

The active contour evolves to minimize the contour energy that includes the internal energy of the contour and the external energy of the image (see Section 2 for details). Applying the variational approach yields internal and external energies associated with the corresponding Euler equations. During the contour deformation process, the internal force maintains the contour smoothness, while the gradient-based external force attracts the contour to the desired boundaries in the image. The deformation finally stops when the snake achieves an energy minimum (force balance). The image noise can attract the snake to a local energy minimum, which does not correspond to the actual object boundaries. Therefore, to reach the desired boundary, the initial contour should lie close to the object to avoid these effects.

With these drawbacks a variety of improvements to the Kass's method have been proposed and implemented.

The most important component of the snake techniques is the gradient based external force, which pushes the snake towards the object boundary. The gradient created nearby the boundary edge must be extended so that the snake feels the object even if it is initialized far from it. This works for both contracting and growing snakes (balloons or artificially inflated contours) proposed in [13,14], where edge-based external forces, enhancing the effect of image edges, have been introduced to overcome the sensitivity to the initial conditions and the noise.

The so-called T-snakes proposed in [15] and their improvements such as the dual T-snakes [16] based on iterative re-parameterization of the original contour are able to make the use of the self-loops. However, the approach allows only "rigid" deformations limited by the superimposed "simplicial grid". An intrinsic internal force that does not depend on contour parameterization based on regularized contour curvature profile has been proposed in [17,18].

In [19] a grammatical framework is proposed to model different local energy models and a set of allowable transitions between these models. The grammatical encodings are utilized to represent a priori knowledge about the shape of the object and the associated signatures in the underlying images.

The sectored snakes proposed in [20] deform the contour with constraints derived from a priori knowledge of the object shape, extracted from the training set of images. This helps the snake to avoid false boundaries and the noise.

Fourier type descriptors have been used in [21] to make the curve evolve to a prescribed shape defined by a template. The

* Corresponding author.
*E-mail address:* smakhanov@yahoo.com (S.S. Makhanov).

0031-3203/$ - see front matter © 2010 Elsevier Ltd. All rights reserved.
doi:10.1016/j.patcog.2010.04.003

prior information is introduced through a set of complete and locally stable invariants to Euclidean transformations (translation, rotation and scale factor) computed using the Fourier Transform.

A probabilistic framework for the region based snake segmentation is introduced in [22]. The observed scene is composed of the target and the background zone with unknown intensities. General statistical solutions for distributions from the exponential family are presented.

In [23,24] region-based image features are combined with the edge-based features incorporated in the external forces. Starting from multiple seeds, Zhu and Yuille [25] performs segmentation of the entire image by iterative boundary deformation and region merging iteratively. However, Ronfard [23] and Chakraborty et al. [24] still require the initial contour to be close to the desired boundary.

A competing approach called the level set method [26] is based on the ideas proposed by Osher and Sethian [27] to use a model of propagating liquid interfaces with curvature-dependent speeds. The interface is a closed, nonintersecting, hyper surface flowing along its gradient field with a constant speed or a speed that depends on the curvature. This is modeled by solving a Hamilton–Jacobi type equation written for a function in which the interface is a particular level set. A speed term derived from the image is used to attach the interface to the object boundaries.

The basic difference between these two models is that the parametric (conventional) models are local methods based on an energy minimizing procedure guided by external forces that pull or push the active contours towards features, such as edges in the image, while the active contours in level set (geometric) models are regarded as the zero level set of a higher dimensional evolving function.

The level set method combined with the contour energy minimization resulted in a variety of the so-called geodesic deformable models, see, for instance, [28–31].

It has been shown in [28,32] that in this framework the minimization of the contour energy is equivalent to minimization of the contour length weighted by an edge detection function in a Riemannian space.

Siddiqi et al. [29] incorporate an area function and the edge function into the length minimization framework to strengthen the contour attracting force.

The minimum description length approach proposed in [33] is based on a deformable partition developed for speckled image composed of a number of homogeneous regions.

Rochery et al. [34] propose a parametric model for higher-order active contours, in particular, quadratic snakes, for extraction of linear structures like roads. The idea is to use a quadratic formulation of the contour's geometric energy to encourage anti-parallel tangents on opposite sides of a road and parallel tangents along the same side of a road. These priors increase the final contour's robustness to partial occlusions, decrease the likelihood of false detections in regions not shaped like roads, and help to prevent self-looping, since different segments of a contour with anti-parallel tangents repel each other in the absence of image forces.

However, the level set representation makes it difficult to impose arbitrary geometric or topological constraints on the evolving contour via the higher dimensional hyper surface [15]. Besides, the level set models may generate shapes having inconsistent topology with respect to the actual object, when applied to noisy images characterized by large boundary gaps [35] requiring exhaustive optimization to accomplish reasonable run times.

Li et al. [36], in reference to the problem of topological adaptation and computational complexity, write "in light of the … inherent weaknesses of geometric active contour models, it is worthwhile to seek solutions within the parametric model realm".

As far as the conventional snake models are concerned, two major modifications must be mentioned: the balloon snakes and the distance snakes.

The balloon snake [13] enables the initial contour to be initialized far from the desired object by adding a constant force, in the external force, to inflate the contour's growth.

The external force field for the distance snake [14] is constructed as the negative of the external energy gradient, which is the distance from each point to its closest edge points in the image. This external energy generated large magnitudes of the external force everywhere in the image, providing a large capture range. Consequently, the initial contour can be located far away from the desired boundary if there are no spurious edges along the way.

Further improvements lie along the lines of processing the underlying vector field rather than modifying the snake model itself. A number of popular codes are based on a gradient vector flow (GVF) method proposed by Xu and Prince [37,38]. A "raw" gradient vector field derived from the image edges is replaced by a vector field that minimizes a certain variational functional. The functional is designed to extend the large gradients far from the boundary, smooth the gradients caused by noise and speckles while keeping gradients attached to strong edges. The corresponding Euler equations represented by linear elliptic PDEs are solved numerically. The PDEs can be also interpreted as the steady state representation of a diffusion process with constant diffusion coefficients.

The generalized gradient vector flow field (GGVF) [39] extends GVF by introducing an analogy with non-uniform diffusion. The GGVF is defined as a steady state solution of a parabolic equation with the elliptic terms and the source term similar to the GVF model. However, the GGVF governing equation employs space varying diffusion, which provides better segmentation accuracy and a larger capture range. Some variations of these ideas are a multidirectional GGVF [40] and a nonlinear diffusion method [41].

GGVF endowed with an appropriate noise elimination remains one of the most popular choices. The GGVF-preprocessed images often allow the snakes to avoid gradients produced by the speckles and the tissue-related edges. However, when the noise related gradients are comparable with the boundary gradients, the diffusion smoothes the false and the true contour points equally. The smoothing after a large number of time steps (iterations) may change the direction of vectors pointing (correctly) towards each other at the true boundary. Although on average GGVF produces a smoother vector field it may also lead to undesirable effects nearby concave boundaries. Besides it may generate such unwanted configurations as the attracting or the repelling stars.

So far the efforts in improving the GGVF method have been focused on appropriate coefficients of diffusion designed to extend the large gradients and remove false boundaries around artifacts. That dual task makes it hard to set up appropriate coefficients for an arbitrary vector field. Theoretically, the iterations should be interrupted when the numerical method converges. However, our experience with US images shows that the result might be "too smooth", so that a part of the object boundary is lost. Therefore, it is often practical to interrupt the iterations before they converge entirely and apply the snake to the resulting vector field. This works well for a series of images with similar properties. However, a new series of images often requires a new setup.

In this paper, we propose a special treatment of the source term of the GGVF equations to improve the accuracy and convergence of the snake subjected to the resulting vector field. Our modification uses intermediate vector fields obtained during the numerical iterations to construct an improved edge map.

The improved edge map is converted back into a new gradient field used in the source term. Consequently, as opposed to the conventional GGVF, where this term is always a function of the original gradient field, our source term is derived from the improved edge map obtained using the numerical solution from a previous iteration.

To be mathematically precise, instead of a single gradient vector field, we consider a sequence of vector fields, where each field derived from the solution at the preceding time step. We demonstrate that our approach provides better convergence and better segmentation accuracy.

The improved vector field is generated from an edge map obtained by a new continuous orientation field analysis inspired by the discrete force field analysis (DOFFA) by Hou and Han [42] presented. DOFFA analyzes relative directions of the gradient field vectors in a $3\times 3$ sliding window to eliminate false contour points produced by the noise.

Our *continuous orientation force field analysis* (COFFA) is based on a numerical measure of a strong edge, applied in a $2\times 2$ window, being rotated around a particular point. This part of the algorithm is similar to oriented filtering (the oriented Gabor filter, the oriented LoG filter, etc.). However, the proposed method differs from the conventional filters. In fact, it is not a filter at all. The COFFA produces a mapping $\varphi(\theta_1,\theta_2)\to[0,255]$, where $\theta_1,\theta_2$ are the positive directions of the gradient vector flow in the opposite nodes of the sample window and $\varphi$ is a measure of how close those directions are to being anti-parallel. Furthermore, $\varphi(\theta_1,\theta_2)$ is considered as a gray level of a new improved image and a new edge map is generated. The new image can be further improved by noise elimination, smoothing, etc. before the edge map is obtained.

The approach has been tested using synthetic low contrast images. It offers a simple computational scheme and leads to a higher segmentation accuracy with reference to the conventional generalized gradient flow method, the balloon snake and the distance snake method. Our numerical experiments on numerous images show similar or better accuracy but at the same time much less sensitivity to the snake controlling parameters and the initial position of the contour as compared to the GGVF snakes, balloon snakes and the distance snakes. Finally, our numerical experiments with medical ultrasound breast images show that the proposed method is more appropriate than the above mentioned methods as applied to segmentation of the breast tumors.

## 2. Gradient vector flow snakes

An active contour or snake parametrically defined as $X(s)=(x(s),y(s))$, $s\in[0,1]$ is a curve that evolves inside the image domain so that it attaches itself to the desired object. The evolution of the snake is governed by Euler equations corresponding to an energy functional defined by

$$E=\frac{1}{2}\int_0^1\left(a\left|\frac{dX}{ds}\right|^2+b\left|\frac{d^2X}{ds^2}\right|^2\right)+E_{ext}(X)\,ds. \tag{1}$$

The minimum of the functional is supposed to be a curve that approximates a boundary of the object of interest. Although this claim has not been proven theoretically for realistic assumptions such as the presence of noise, false objects, speckles, low contrast areas, etc., a strong rationale behind it is the variational functional (1).

The first term establishes an equidistribution of points along the resulting curve whereas the second term ensures against large curvatures. The weighting parameters $a$ and $b$ are to control the snake's tension and rigidity. Finally, $E_{ext}$ is the external energy that pulls the snake towards the desired object boundaries. The simplest choice of $E_{ext}$ is a magnitude of the gradient of the gray level subjected to a Gaussian filtering. However this option is rarely acceptable since it provides a very small capture range and is sensitive to the noise. Conventional smoothers such as the Laplacian applied to the gradient fields may remove some noise, but they also may destroy the true boundary. In particular, ultrasound (US) images of the breast tumors could be very noisy with speckles and tissue related textures obstructing the actual tumor. Consequently, $E_{ext}$ does not perform well on them. In particular, the snakes are displaying poor convergence into the concavities of the boundary due to the small capture range.

A very popular extension of the gradient field approach is the so-called gradient vector flow (GVF) originally proposed by Xu and Prince [37,38]. The technique replaces a "raw" gradient vector field derived from the image edges by a vector field which minimizes a certain functional which extends the large gradients far from the boundary and smoothes the gradients caused by noise. The GVF is a solution of a linear elliptic equation given by

$$\mu\nabla^2V-(V-\nabla f)|\nabla f|^2=0, \tag{2}$$

where $\nabla f$ is the gradient field derived from the edge map of the image. Eq. (2) is the Euler equation for the following functional:

$$\mu\int\int(u_x^2+u_y^2+v_x^2+v_y^2)\,dx\,dy+\int\int|\nabla f|^2(V-\nabla f)^2\,dx\,dy. \tag{3}$$

The first integral produces a smoothly varying vector field $V=(u(x,y),v(x,y))$, while the second integral encourages the vector field to approach $\nabla f$ where $|\nabla f|$ is large. Furthermore, Eq. (2) is solved by treating $V$ as a function of a pseudo-time and by performing numerical iterations with regard to the pseudo-time as follows:

$$V^{n+1}=V^n+\tau'(\mu\nabla^2V-(V-\nabla f)|\nabla f|^2)^n, \tag{4}$$

where $n$ is the iteration number and $\tau'$ is the iteration parameter (a step along the pseudo-time). Note that, iterations (4) can be interpreted as solving numerically a heat equation given by

$$\frac{\partial V}{\partial t}=\mu\nabla^2V-(V-\nabla f)|\nabla f|^2. \tag{5}$$

However, the uniform diffusion $\mu$ often produces excessive smoothing. Therefore, Xu and Prince [39] extended the GVF technique by introducing spatially varying coefficients to decrease the smoothing effect, namely,

$$\frac{\partial V}{\partial t}-g(|\nabla f|)\nabla^2V-h(|\nabla f|)(\nabla f-V)=0. \tag{6}$$

The improved version of the GVF is called the generalized gradient vector flow (GGVF). The weighting functions $g$ and $h$ depend on the gradient of the edge map so that in the proximity of large gradients $g$ gets smaller whereas $h$ becomes larger. In [39] the following weighting functions have been proposed

$$g(|\nabla f|)=e^{-(|\nabla f|/K)},\quad h(|\nabla f|)=1-g(|\nabla f|), \tag{7}$$

where $K$ is a calibration parameter.

Note that parabolic equations (5) and (6) require boundary conditions and an initial condition given by $V(x,y,0)=\nabla f(x,y)$.

An obvious choice is the Neumann boundary condition

$$\frac{\partial V}{\partial N}|_\Gamma=0,$$

where $\Gamma$ is the boundary of the image rectangular region and $N$ is the outward normal (some care must be taken at the corners of the rectangle). In the framework of the heat equation analogy it means that the "flux of $V$" through the boundary is constant along the normal. Furthermore, the Dirichlet boundary condition

$$V|_\Gamma=V_\Gamma$$

may have undesirable effects on the solution. Finally, the Robin (or the third type) boundary condition is hard to interpret in the GVF sense.

As mentioned above the GVF produced by iterations (4) may be "under-iterated" when the gradients are not extended far enough from the actual boundary of the object or "over-iterated" when the true boundary is partially destroyed by an excessive smoothing.

The smoothing effect depends on the diffusion coefficient $\mu$ (or $K$ in case of (7)) and the iteration step $\tau'$. The solution may be affected by the numerical diffusion as well (a question that has been never discussed with regard to the GVF models). If a conventional stopping criterion based on the proximity to the steady state solution produces an "over-smoothed" solution, the user must modify the diffusion coefficient or interrupt the iterations earlier. However, interrupting the iterations too early may lead to false boundaries and artifacts.

Consider an introductory example. A one-dimensional version of (6) is given by

$$\frac{\partial V}{\partial t} - g(\nabla f)\frac{\partial^2 V}{\partial x^2} + h(\nabla f)(V - \nabla f) = 0,$$
$$\frac{dV}{dx}(0,t) = 0, \frac{dV}{dx}(1,t) = 0, \tag{8}$$

$V(x,0) = \nabla f$, where $V = V(x,t)$, $0 \le x \le 1$.

In the one-dimensional case $\nabla f \equiv (df(x)/dx)$.

Consider a GVF characterized by $g \equiv \mu$, $h \equiv 1$ with $\nabla f$ given by

$$\nabla f = 1.2(0.4-x)e^{-2500(x-0.4)^2} + (0.6-x)e^{-2500(x-0.6)^2} + 0.2\sin(100x). \tag{9}$$

The curve emulates a 1D "object" placed between 0.4 and 0.6 characterized by a sharp change of $\nabla f$ from positive to negative at the object boundary (see also Fig. 1(a)). The oscillating term $0.2\sin(100x)$ imitates the "noise". Fig. 1(b), (c) and (d) depicts the solutions of (8) and (9) with the Neumann boundary condition for various diffusion coefficients.

Clearly, $\mu = 0.0001$ (Fig. 1(b)) is too small. Consequently, the noise generates vector field artifacts, which may attract the snake to a false boundary. Furthermore $\mu = 0.001$ (Fig. 1(c)) generates an acceptable solution. The gradient has been extended enough so that even if the snake is initialized far from the object, it still will be attracted. Finally, $\mu = 0.05$ (Fig. 1(d)) produces an "over-smoothed" solution. The object virtually disappears as the result of an excessive diffusion. Therefore, such $\mu$ is totally unacceptable.

Space varying coefficients (7) introduced by GGVF offer another way to control the vector field. The GGVF is illustrated by numerical solutions of (8) and (9) with $g(\nabla f) \equiv e^{-|\nabla f|^2/K}$, $h(\nabla f) = 1 - g(\nabla f)$ for $K = 0.01$, 0.3 and 0.1. Clearly, the three outcomes considered above are still possible. Small diffusion induced by $K = 0.01$ (Fig. 2(a)) creates artifacts, whereas large $K = 0.3$ destroys the object (Fig. 2(b)). However, an appropriate diffusion $K = 0.1$ generates a good vector field (Fig. 2(c)) where the noisy parts have been eliminated while the large edges remain intact and have been extended far from the object.

However, the result in figure (b) can be improved if the original gradient field $\nabla f$ is replaced by a modified gradient $\nabla f_s$ which uses solutions obtained at previous time steps. For instance, the solution depicted in figure (d) has been obtained using in (8) and (9) a sequence of gradient vector flow vectors given by

$$\nabla f_s(x) = \begin{cases} \nabla f & \text{if } t = 0, \\ V(x,t-s) & \text{if } t > 0, \end{cases} \tag{10}$$

where $s$ is the delay.

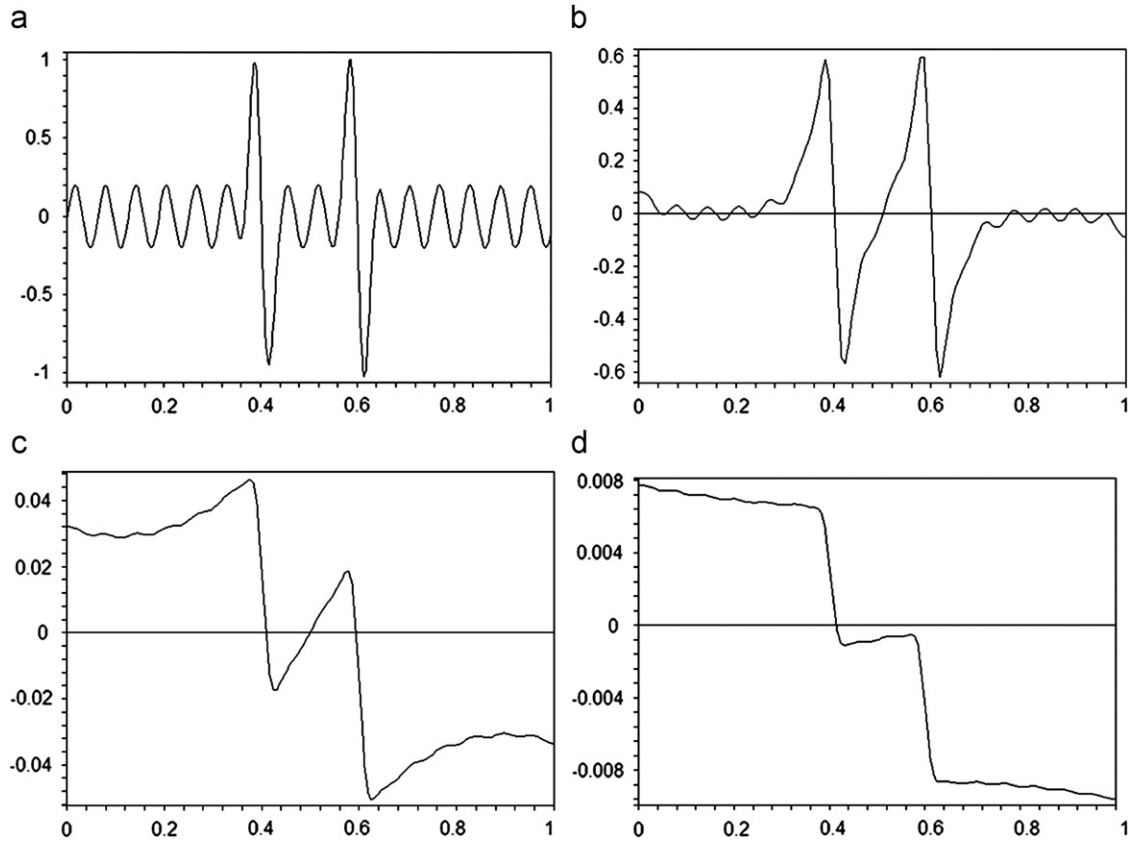


**Fig. 1.** 1D simulations of the GVF: (a) the gradient curve, (b), (c) and (d) solutions of equation (8) with $\mu = 0.0001$, 0.001 and 0.05.

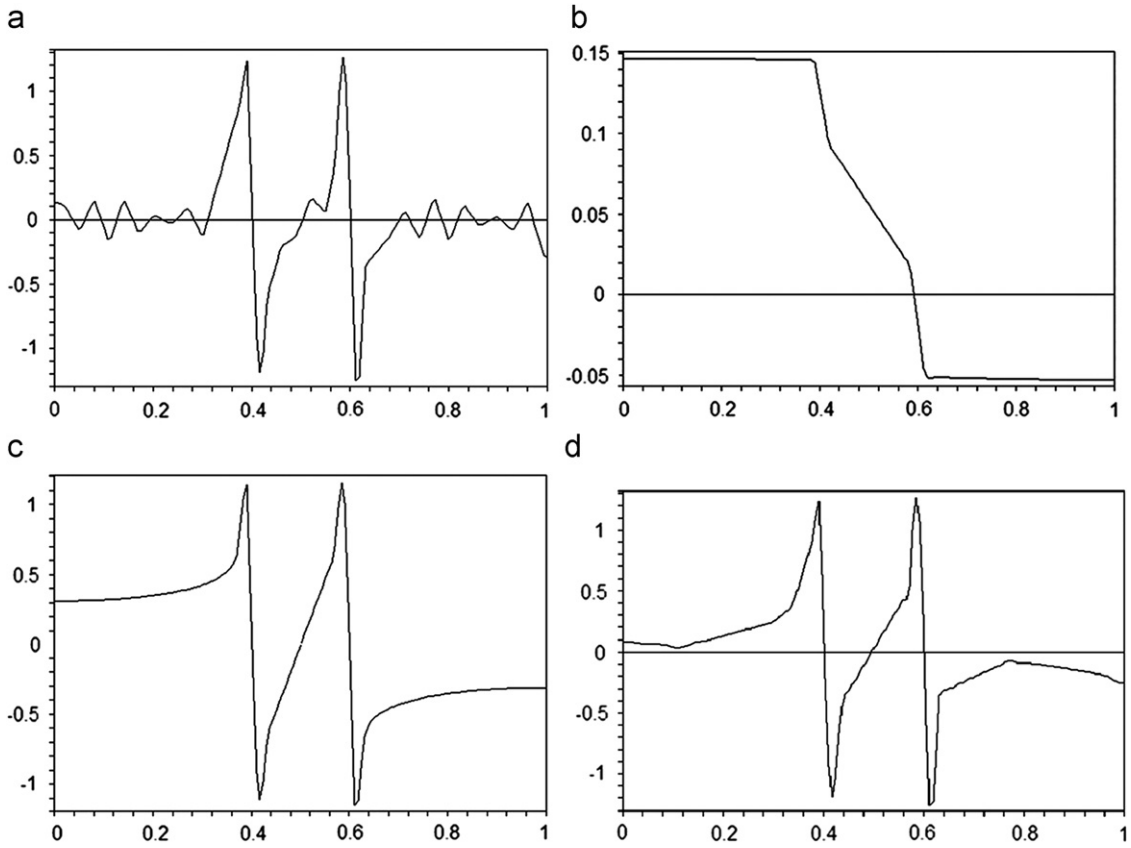


**Fig. 2.** 1D simulations of the GGVF: (a) small diffusion, (b) large diffusion, (c) appropriate diffusion and (d) modified GGVF with large diffusion.

Note, that introducing (10) replaces linear boundary value problem (8) and (9) by a nonlinear one; however, in many cases it improves the convergence and the subsequent segmentation accuracy.

Generalization of these techniques to 2D images is not straightforward. Therefore, the next section introduces continuous orientation force field (COFFA) analysis techniques and its use in the framework of GGVF.

## 3. Continuous orientation force field analysis

The main idea of the discrete orientation force field analysis (DOFFA) proposed by Hou and Han [42] is that the true boundary vectors must face each other along a certain direction. Therefore, DOFFA introduces a $3\times 3$ sampling window around the candidate boundary point and analyses the directions of the vector field in this window. This procedure is illustrated in Fig. 3.

Positions (1)–(4) and sixteen positions (5)–(8) including rotations and symmetry in Fig. 3 constitute the basic configuration of DOFFA. However, DOFFA introduces many other positions such as the broken point (9) and (10) and others. It is not clear whether the set of positions is complete. Of course, for the real image the vectors are not precisely anti-parallel. Therefore, the procedure is based on a certain threshold which is often hard to define. Consider Fig. 3(11). When the vectors are positioned inside sectors A and B, respectively, they are taken by DOFFA as anti-parallel; however, when at least one vector is outside the prescribed sector, the decision reverses. Clearly, the threshold for such binary assignment is not easy to find. For instance, when the boundary is noisy, the vectors may considerably deviate from the standard anti-parallel positions. Besides, in the case of an iterative use of GGVF the threshold may create divergence since numerical methods for PDE in general do not perform well when some terms are not smooth (switch between different states).

In this paper, we modify and extend the DOFFA-techniques as follows. In order to decrease the number of vectors to compare we employ a $2\times 2$ *rotating* window (see Fig. 7(a)). The smaller size is compensated for by rotations, which make it possible to accurately capture the directions of the vector field around the candidate point. Observe that DOFFA is very hard to extend to larger windows. Even for a window $5\times 5$ the number of configurations indicating a possible boundary is hard to derive and interpret. As opposed to that, our method applies to an arbitrary window size.

The most important difference though is a continuous measure $\varphi(\theta_1,\theta_2)$ employed instead of the binary rules of DOFFA. In other words, instead of deciding whether the vectors are anti-parallel, we introduce a measure that evaluates a deviation from an ideal anti-parallel position. The measure is then used to generate a score vector.

For each orientation of the window the vector field is first interpolated into the corners of the window (Fig. 7(b)). Next, $\varphi(\theta_1,\theta_2)$ measures the deviation of the vectors at the two opposing corners from the direction corresponding to the orientation of the window. The closer the two vectors are to the prescribed direction, the greater is $\varphi(\theta_1,\theta_2)$.

The maximum response $\varphi(\theta_1,\theta_2)$ shows how close to the anti-parallel position the vector field is in the locality of the candidate boundary point. In order to construct the membership function $\varphi(\theta_1,\theta_2)$ we use simple two dimensional interpolation techniques with a few control points. The measure $\varphi(\theta_1,\theta_2)$:$([0,2\pi]\times[0,2\pi])\rightarrow[0,1]$ is first constructed on a triangle $\{(0,(\pi/2)),((\pi/2),(\pi/2)),((\pi/2),\pi)\}$ using interpolating points at the corners and in

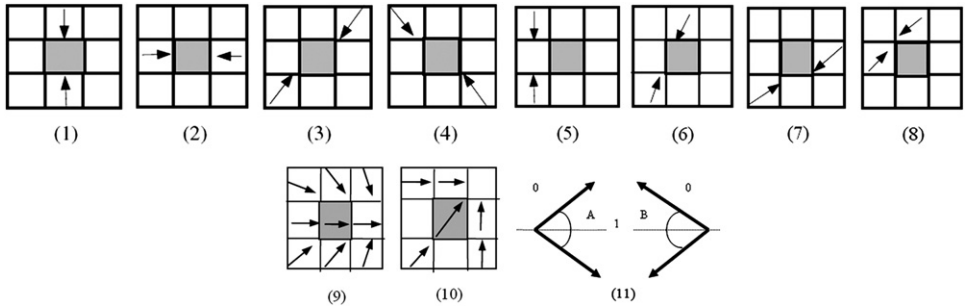


**Fig. 3.** Basic vector configurations for the discrete orientation force field analysis (DOFFA).

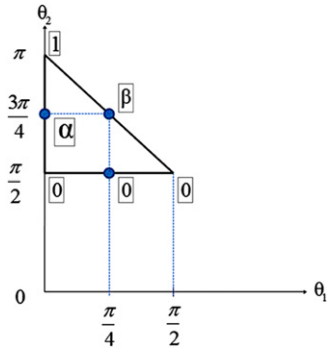


**Fig. 4.** The "basic" triangle to define $\varphi(\theta_1,\theta_2)$, the $\varphi$-values are indicated by the frames.

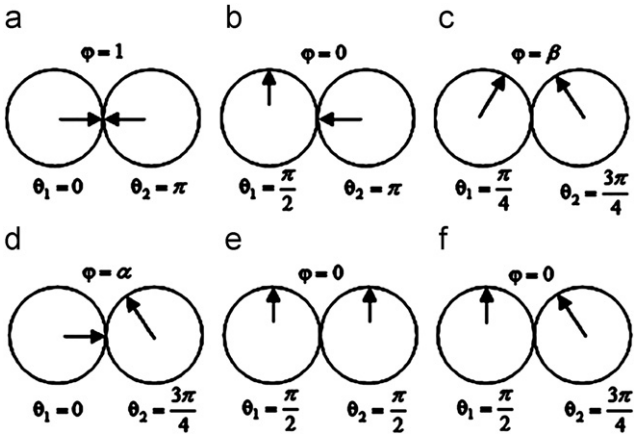


**Fig. 5.** (a)–(f) The standard positions.

the middle of each side of the triangle (Fig. 4). The following conditions at the interpolating points are used:

$$\varphi(0,\pi)=1,\ \varphi\left(\frac{\pi}{2},\pi\right)=0,\ \varphi\left(\frac{\pi}{4},\frac{3\pi}{4}\right)=\beta,\ \varphi\left(0,\frac{3\pi}{4}\right)=\alpha,\ \varphi\left(\frac{\pi}{2},\frac{\pi}{2}\right)=0,\ \varphi\left(\frac{\pi}{2},\frac{3\pi}{4}\right)=0,$$

where $\alpha$ and $\beta$ are the design values (see Fig. 5(a)–(f), respectively).

Suppose that $\varphi(0,(3\pi/4))=\alpha=0.5$ (Fig. 5(d)). It means that the measure of position (d), deviating from the ideal position by $\frac{\pi}{4}$, is 50% of what we assign in the ideal case when the deviation is zero.

Furthermore, the six positions define a quadratic polynomial given by

$$\varphi(\theta_1,\theta_2)=a_1\theta_1^2+a_2\theta_1\theta_2+a_3\theta_2^2+a_4\theta_1+a_5\theta_2+a_6. \quad (11)$$

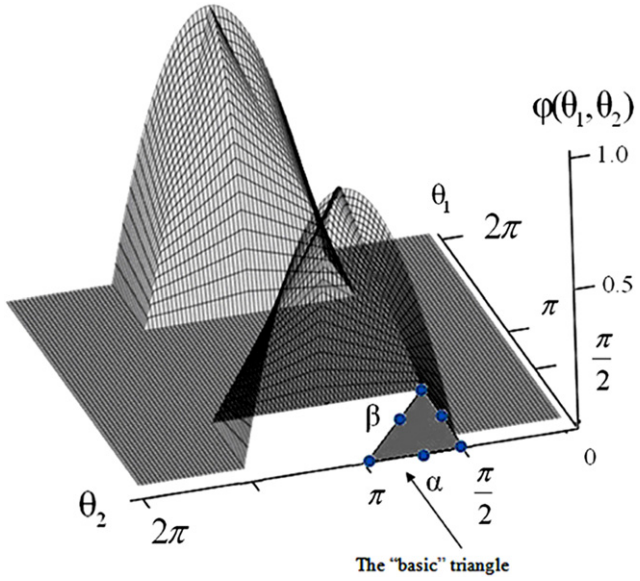


**Fig. 6.** The membership function (10) extended to the entire domain $[0,2\pi]\times[0,2\pi]$.

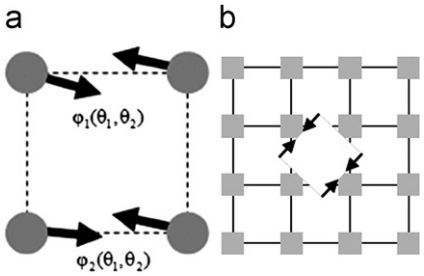


**Fig. 7.** (a) The $2\times2$ window and (b) the rotating $2\times2$ window.

Once coefficients $a_i$ are evaluated from (11), $\varphi(\theta_1,\theta_2)$ is extended to $[0,2\pi]\times[0,2\pi]$ symmetrically as shown in Fig. 6, thus becoming a piecewise quadratic function.

Note, that if $\alpha=\beta=1/2$, then $\varphi(\theta_1,\theta_2)$ becomes a bilinear function given by $(1-(2/\pi)\theta_1)(1-(2/\pi)\theta_2)$. Furthermore, $\varphi(\theta_1,\theta_2)$ applies to rotating window $W_\gamma$ (Fig. 7) to produce a sequence of two dimensional score vectors $s_\gamma=(\varphi_1,\varphi_2)_\gamma$, where $\gamma$ is the rotation angle.

The vectors are normalized as follows: $s_{\gamma,new}=(s_\gamma/(\max|s_\gamma|))$. We assume that the true contour points form large clusters characterized by $|s_\gamma|>1-\delta$, where $\delta$ is an appropriate threshold. Besides the true boundary points must belong to relatively large

continuous segments, whereas the false contour points belong to short segments. Consequently, appropriate edge detection methods such as [43–45] can be applied.

Finally, mapping $|s_\gamma|$ linearly onto [0,255] for every pixel constructs a new gray level image. The image is processed further and a new gradient field is derived from that image again.

The proposed procedure can be generalized by considering an arbitrary or varying number of pairs of points defined along the opposite sides of the sampling window. The window may also have a varying width to height ratio. The proposed algorithm could be also combined with the linear phase portrait analysis (see, for instance, [46]) or even nonlinear phase portrait [47,48].

## 4. Iterative algorithm

As mentioned in the introduction, GVF as well as GGVF may be under-smoothed when the gradients are not extended far enough from the actual boundary or over-smoothed, when the true boundary is partially or even entirely destroyed by smoothing.

We will prove experimentally that the convergence to a "good" solution can be improved if the "raw" gradient field $\nabla f$ in equation (5) is replaced by $\nabla f'$ where $f'$ is an adaptive edge map obtained by COFFA.

The algorithm consists of the following steps:

1. Apply the GGVF to the raw gradient field $\nabla f$ to obtain $V(x,y)=(u(x,y),v(x,y))$.
2. Apply COFFA to the resulting $V(x,y)$ to obtain the score vector $s(x,y)=(\varphi_1,\varphi_2)$.
3. Convert $s(x,y)$ into a new gray level image $\tilde{f}(x,y)$.
4. Threshold the gray level image to obtain a COFFA image $f'(x,y)$ (the adaptive edge map).
5. Calculate the gradient field of the COFFA image $\nabla f'(x,y)$.
6. Replace the raw gradient field by the new gradient field obtained and use it for the next series of iterations for numerical solution of Eq. (6).
7. Check for convergence and go to 2 if necessary.
8. Run the snake on the final COFFA-GGVF.

Step 4 requires some comments. The image is thresholded based on the magnitude of the gradient and stability of the edge. If $f>T_1$ then the gray level at that point is incremented; if $f<T_2$, then it is decremented. Finally, if $T_1\geq f\geq T_2$, the decision is made based on the edge stability, namely, if $|f-\tilde{f}|<\varepsilon$, where $\varepsilon$ is a prescribed tolerance (the edge is stable), then it is incremented, otherwise it is decremented.

Observe that the snake can also be evolved within the COFFA-GGVF iterations. In many cases this approach leads to impressive results. However, a correct combination of the evolution of the vector field and the snake is still an open problem. Note that evaluation of the COFFA image for every iteration slows down the algorithm. Besides it may lead to divergence of the numerical solution. Therefore, similar to the delayed source term in (8) and (9) we calculate the new gradient field at each $n'$th iteration, where $n'$ is the calibration parameter.

The entire list of the algorithm's parameters and their numerical values producing appropriate results for our series of the medical US images are given below:

1) The diffusion coefficient (GGVF) $K\approx 0.1$.
2) The time step for numerical solution of the parabolic equation (5) $\tau\leq 10$.
3) The design parameters for the membership function (10): $\alpha=0.5$, $\beta=0.5$.
4) The upper and lower threshold for creating the gray level COFFA image can be found by the Otsu algorithm [50].

Note that the problem of finding thresholds $T_1,T_2$ is in fact a problem of finding clearly strong ($f>T_1$) and clearly weak ($f<T_2$) edges. Pixels, characterized by $T_1\geq f\geq T_2$, are treated using the notion of edge stability. The idea is similar to Lindeberg's space-scale edge detection [51]. The stronger the edge, the longer it survives under smoothing effects of the diffusion. The similarity of the space-scale Gaussian blurring and diffusion produced by the GFV is also transparent, since a Gaussian is a solution of Eq. (5) if the term $(V-\nabla f)|\nabla f|^2$ is neglected.

As far as the thresholds $T_1,T_2$ are concerned, they can be found by histogram based methods such as the Otsu algorithm or even adjusted manually. Conservative estimates do not significantly affect the algorithm, since the missing strong edges will be later discovered by the stability criteria. However, it is our experience that the Otsu method usually provides a relatively robust upper and lower threshold.

Furthermore, we present numerical experiments performed on a series of synthetic images as well as on actual digital US images of breast tumors.

## 5. Numerical experiments: synthetic images

The accuracy is defined as a percentage of true positive points with reference to the true boundary. A contour point is considered to be a true positive point if a point in the ground truth image belongs to the true contour.

The accuracy is also evaluated in terms of the generic Hausdorff distance given by

$$dist_H(X_1,X_2)=\max\{\max_{a\in X_1}\min_{b\in X_2}||a-b||,\max_{b\in X_2}\min_{a\in X_1}||a-b||\}, \tag{12}$$

where $\|\cdot\|$ denotes the Euclidian distance, $X_1$ the resulting contour and $X_2$ the ground truth. In order to obtain a dimensionless estimate, the Hausdorff distance is divided by the length of the true contour $L_{X_2}$ as follows:

$$dist_{H,norm}(X_1,X_2)=\frac{dist_H(X_1,X_2)}{L_{X_2}}. \tag{13}$$

Measure (13) is a ratio of the maximum distance between the snake and the true contour and the length of the true contour. For instance, the difference in 10 pixels is significant if the perimeter of the object is 100 pixels (a small object) but might not be that important if the length is 10 000 pixels (a large object). Furthermore, the advantage of (12) and (13) is that it is a distance in a mathematical sense, whereas the number of true positives is not. A combination of the true positives and the Hausdorff distance is a good measure of the segmentation quality. A larger degree of overlap of the boundaries (true positives) signifies a better segmentation. On the other hand, if the number of true positives is equal to zero, the boundaries could still be close, say at the distance of one pixel. In that case the Hausdorff distance shows that the quality of segmentation is still relatively good. In turn, a set of boundaries dissimilar only over small portions may have the same Hausdorff distance as that of the globally dissimilar set of boundaries. However, if the boundaries are globally dissimilar we may expect a very low number of true positives. Finally, if the number of true positives is high and the Hausdorff distance is low, the quality of segmentation is very likely to be good.

We also evaluate the robustness of the method by its numerical convergence.

Let $T_n$ be the number of true positives and let $X_n$ be the snake contour at iteration $n$. If for some $n$ and $k_0$

$$|T_{n+k}-T_n| < \varepsilon_T \text{ and } \frac{|dist_{H,norm}(X_{n+k},X_n)-dist_{H,norm}(X_{n+1},X_n)|}{dist_{H,norm}(X_{n+1},X_n)}100 < \varepsilon_H, \forall k \le k_0, \quad (14)$$

we will say that the method converges. Here, $k_0$ is the number of iterations during which the accuracy estimates are stable and $\varepsilon_T$, $\varepsilon_H$ the required tolerance. Note, that although definition (14) is mathematically correct, an appropriate criteria of convergence of the GGVF snakes is still an open problem [52].

**Example 1.** Simple geometric figures. Gaussian noise. Large diffusion.

The snake is initialized around a triangle in the center of an image in Fig. 8 subjected to a 2% Gaussian noise. Fig. 8(b) shows that the snake using COFFA-GGVF is able to attach itself to the boundary of the object. However, the same diffusion coefficient employed by a conventional GGVF leads to an unacceptable result (Fig. 8(a)).

Table 1 compares the two methods with varying $K$ and the distance snake (DS) method. The two numbers in the cells of the table correspond to the percentage of the true positives and

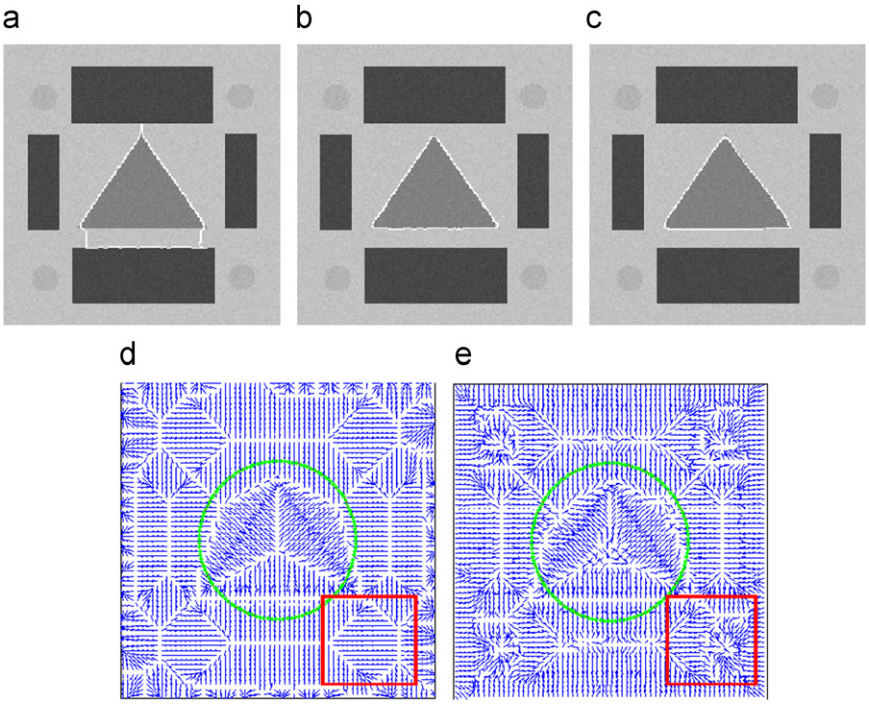


**Fig. 8.** Snake based segmentation using (a) the conventional GGVF, (b) the COFFA-GGVF, $K=0.4$ (c) the distance snake (DS), $T=0.313$, (d) the gradient vector field corresponding to the distance snake method and (e) gradient vector field obtained by COFFA-GGVF.

**Table 1**
Accuracy (percentage of true positives and the Hausdorff distance) of GGVF, COFFA-GGVF and DS. 2% noise. Image in Fig. 8.

| Method/iterations | GGVF $K$ | | | COFFA-GGVF $K$ | | | DS $T=0.313$ |
|---|---|---|---|---|---|---|---|
| | 0.01 | 0.1 | 0.4 | 0.01 | 0.1 | 0.4 | |
| 10 | 79.613<br>0.030 | 78.847<br>0.030 | 76.820<br>0.030 | 79.808<br>0.029 | 79.817<br>0.029 | 79.458<br>0.029 | 89.287 |
| 30 | 88.293<br>0.005 | 85.222<br>0.008 | 82.123<br>0.013 | 89.125<br>0.004 | 89.176<br>0.004 | 88.493<br>0.006 | 0.004 |
| 50 | 88.711<br>0.005 | 86.258<br>0.008 | 69.755<br>0.034 | 89.125<br>0.004 | 89.176<br>0.004 | 87.725<br>0.006 | |
| 70 | 88.755<br>0.005 | 85.641<br>0.009 | 69.755<br>0.034 | 89.125<br>0.004 | 89.176<br>0.004 | 87.725<br>0.006 | |
| 90 | 88.705<br>0.005 | 74.609<br>0.035 | 54.725<br>0.034 | 89.125<br>0.004 | 89.176<br>0.004 | 87.725<br>0.006 | |
| 110 | 88.421<br>0.005 | 74.184<br>0.035 | 54.095<br>0.034 | 89.125<br>0.004 | 89.176<br>0.004 | 87.362<br>0.006 | |
| Converg. | Yes | No | No | Yes | Yes | Yes | |

the normalized Hausdorff distance (13). In what follows our convergence criterion (14) employs $k_0=20$, $\varepsilon_T=\varepsilon_H=0.25\%$. In other words the difference in the number of true positives and between the consecutive snake contours in terms of the distance (13) must not be larger than 0.25% during at least 20 iterations. Moreover, we require that the result produces the best accuracy for both: the true positives and the Hausdorff distance during the entire iteration process. For example, if the best snake during the iterations consists of 95% true positives but the iterations converge in the sense (14) to a snake having 90% true positives, we consider this a divergence because the snake was in a better position but failed to converge to it.

Clearly, COFFA-GGVF displays a better accuracy and a larger range of acceptable diffusion coefficients, whereas GGVF diverges for $K=0.1$ and $K=0.4$. The DS displays a slightly better accuracy; however, the resulting vector field obtained with Otsu threshold [49] does not contain vectors attracting to the gray balls at the corners of the picture, whereas COFFA-GGVF still contains the objects. Our forthcoming examples show that the DS does not perform better on complex objects even with a manually adjusted threshold, whereas COFFA-GGVF works fine with Otsu thresholding.

Furthermore, Table 2 shows that COFFA-GGVF is more resistant to noise than the classic GGVF. For instance, the performance of GGVF for $K=0.01$ dropped by 10% with the increase of noise by 1.5% whereas the performance of COFFA-GGVF dropped only by 5%.

**Table 4**
Accuracy for different incorporated edge detection methods. Image in Fig. 9(a).

| Method | GGVF | COFFA-GGVF | DS |
|---|---|---|---|
| Prewitt | 77.667<br>0.018 | 83.837<br>0.007 | 66.932<br>0.076 |
| Sobel | 77.812<br>0.018 | 84.511<br>0.006 | 67.416<br>0.077 |
| Canny | 78.019<br>0.016 | 84.610<br>0.005 | 68.213<br>0.043 |

**Table 2**
Accuracy: GGVF, COFFA-GGVF and DS. 3.5% noise. Image in Fig. 8; 110 iterations.

| Method/estimate | GGVF $K$ | | | COFFA-GGVF $K$ | | | DS snake $T=0.302$ |
|---|---|---|---|---|---|---|---|
| | 0.01 | 0.1 | 0.4 | 0.01 | 0.1 | 0.4 | |
| The best | 80.1310<br>0.0319 | 86.3320<br>0.0088 | 81.0440<br>0.0130 | 86.7270<br>0.0088 | 86.1270<br>0.0088 | 85.8040<br>0.0088 | 87.6740<br>0.0088 |
| The worst | 67.2920<br>0.0331 | 64.6090<br>0.0299 | 47.1660<br>0.0381 | 79.3830<br>0.0245 | 79.4690<br>0.0381 | 78.9000<br>0.0312 | |
| Converg. | No | No | No | Yes | Yes | Yes | |

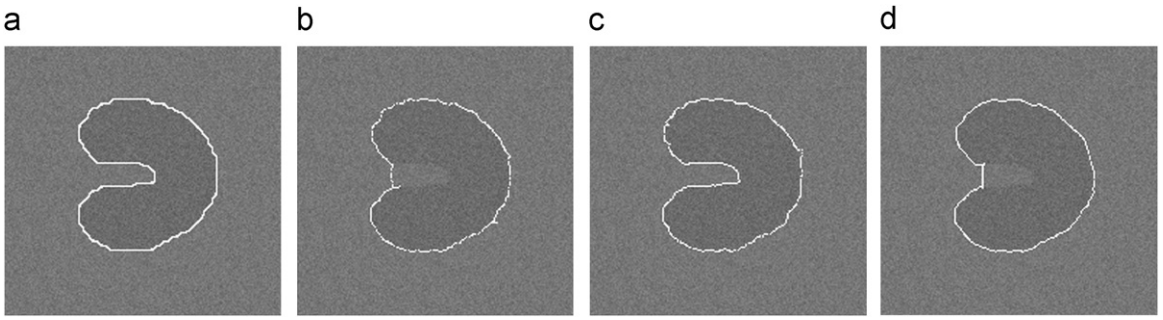


**Fig. 9.** (a) The ground truth, (b) conventional GGVF (110 iterations), (c) COFFA-GGVF(110 iterations), $K=0.01$ and (d) distance snake, $T=0.1$.

**Table 3**
Accuracy: GGVF, COFFA-GGVF and DS, 2.5% noise. Image in Fig. 9(a); 150 iterations; Prewitt edge detection, "Yes*" denotes convergence to a reasonably good but not the best solution.

| | GGVF $K$ | | | COFFA-GGVF $K$ | | | DS $T=0.1$ |
|---|---|---|---|---|---|---|---|
| | 0.01 | 0.1 | 0.4 | 0.01 | 0.1 | 0.4 | |
| The best | 65.751<br>0.077 | 77.667<br>0.018 | 76.019<br>0.018 | 81.102<br>0.008 | 83.837<br>0.007 | 82.859<br>0.010 | 66.932<br>0.076 |
| The worst | 62.543<br>0.077 | 68.436<br>0.028 | 53.283<br>0.028 | 77.047<br>0.069 | 79.976<br>0.018 | 80.522<br>0.018 | |
| Converg. | Yes | No | No | Yes*<br>80.727<br>0.007 | Yes | Yes | |

Note that Table 2 and all the forthcoming tables show only the best and the worst results in each category and whether the method *converges numerically in the sense* (14) *to the best value.*

**Example 2.** Horseshoe shape. Small diffusion.

**Table 5**
The accuracy with varying distance of the initial contour from the true boundary (robustness test). Image in Fig. 9(a).

| Distance | GGVF | COFFA-GGVF | DS |
|---|---|---|---|
| 2.4 | 77.667<br>0.018 | 83.837<br>0.007 | 66.932<br>0.076 |
| 3.6 | 71.341<br>0.030 | 80.137<br>0.016 | 66.584<br>0.077 |
| 6.0 | 60.475<br>0.045 | 79.617<br>0.024 | 66.462<br>0.079 |

The experiment compares GGVF and COFFA-GGVF applied to a synthetic, low contrast image and an object with a concave boundary subjected to a Gaussian noise of about 2.5% (Fig. 9).

The experiments (Table 3) show that the vector fields constructed with a low diffusion are unable to attract the snake to the concave boundary due to small gradients and the presence of noise. However, our version of GGVF is able to develop gradients capable of attracting the snake into the concavity *without additional corrections* often required for such configurations [39]. Note that when $K$ is small, GGVF does not "feel" the concavity whereas for average and large $K$, GGVF does not converge. Consequently, COFFA-GGVF outperforms GGVF for almost every $K$. The distance snake displays a low performance even with the best threshold obtained manually.

Furthermore, we incorporate three popular edge detection algorithms, namely, Prewitt [43], Sobel [45] and Canny edge detection [44]. We test them using the trial and error approach

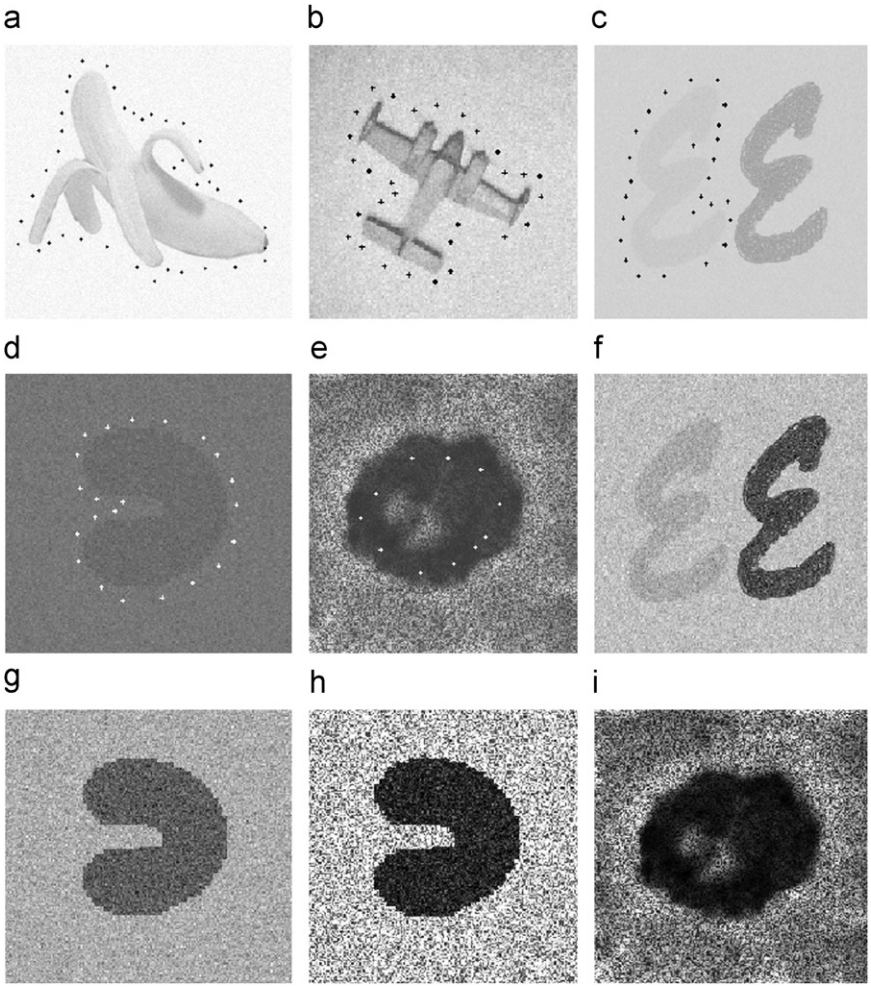


**Fig. 10.** Test images (a) banana, (b) plane, (c) letter E, (d) horseshoe-Gaussian noise, (e) synthetic "tumor"—speckle noise, (f) letter E scaled to [0,1], (g) horseshoe-Gaussian noise scaled to [0,1], (h) horseshoe, speckle noise scaled to [0,1] and (i) synthetic "tumor", speckle noise, scaled to [0,1].

**Fig. 11.** A series of sheared and twirled image "banana".

**Table 6**
Average accuracy. Series of images in Figs. 10 and 11, *—an Otsu threshold, **—the best threshold.

| Method/series | GGVF | COFFA-GGVF | DS | BS |
|---|---|---|---|---|
| Banana series | 85.106<br>0.009 | 86.443<br>0.006 | 69.819<br>0.025*<br>79.197<br>0.019** | 75.667<br>0.018 |
| Plane series | 78.565<br>0.009 | 79.517<br>0.008 | 78.883<br>0.015 | 56.276<br>0.017 |
| E-series | 68.428<br>0.019 | 91.450<br>0.013 | 40.850<br>0.023 | 72.239<br>0.021 |
| Horseshoe series | 70.162<br>0.023 | 80.261<br>0.010 | 66.231<br>0.067 | 60.417<br>0.081 |
| Horseshoe series, speckle noise | 69.529<br>0.013 | 85.940<br>0.005 | 52.029<br>0.023 | 59.511<br>0.037 |
| Synthetic tumor, speckle Noise | 76.047<br>0.021 | 96.302<br>0.003 | 51.936<br>0.007 | 54.094<br>0.011 |

and combine them with GGVF, DS and COFFA-GGVF. Table 4 shows that the performance of COFFA-GGVF is the best irrespective of the underlying edge detection procedure.

Next, the accuracy is evaluated with a varying Hausdorff distance (12) between the initial contour and the true boundary (the robustness test). The initial contour evolves from a small circle initialized inside the object. The contour is subjected to the GGVF snake routine until it reaches a certain distance from the boundary. Finally, the contour is used as the initial one on the actual noisy image. The accuracy of COFFA-GGVF and DS practically does not depend on distance; however, the accuracy of the DS is low since it cannot resolve the concavity without additional modifications of the algorithm. Observe that it has been demonstrated in many works (for instance [37]) that the GGVF snake enters the concavity of the horseshoe-shaped image and accurately attaches itself to the actual boundary. However, when the noise is present, GGVF does not perform that well. Table 5 shows that with a 2.5% noise the accuracy of GGVF drops by 11% when the initial contour is at a 6 pixel distance from

**Table 7**
Average accuracy. Series of images in Figs. 10 and 11.

| Method/series | Distance (pixels) | GGVF | COFFA-GGVF | DS | BS |
|---|---|---|---|---|---|
| Banana series | 5.7 | 85.106<br>0.009 | 86.443<br>0.006 | 79.197<br>0.019 | 75.667<br>0.018 |
| | 10.3 | 74.328<br>0.016 | 86.446<br>0.006 | 66.819<br>0.020 | 49.308<br>0.019 |
| Plane series | 4 | 78.565<br>0.009 | 79.517<br>0.008 | 78.883<br>0.015 | 56.276<br>0.017 |
| | 6.7 | 77.040<br>0.012 | 78.003<br>0.009 | 77.658<br>0.015 | 31.602<br>0.022 |
| E-series | 4.5 | 68.428<br>0.019 | 91.450<br>0.013 | 40.850<br>0.023 | 72.239<br>0.021 |
| | 8 | 42.808<br>0.032 | 74.984<br>0.020 | 27.606<br>0.028 | 43.745<br>0.027 |
| Horseshoe series | 3.5 | 70.162<br>0.023 | 80.261<br>0.010 | 66.231<br>0.067 | 60.417<br>0.081 |
| | 6.0 | 60.203<br>0.047 | 78.011<br>0.029 | 63.410<br>0.059 | 49.93<br>0.084 |
| Horseshoe series, speckle noise | 3.5 | 69.529<br>0.013 | 85.940<br>0.005 | 52.029<br>0.023 | 59.511<br>0.037 |
| | 6.0 | 58.712<br>0.034 | 80.088<br>0.023 | 50.16<br>0.048 | 47.142<br>0.059 |
| Synthetic tumor series, speckle noise | 4.0 | 76.047<br>0.021 | 96.302<br>0.003 | 51.936<br>0.007 | 54.094<br>0.011 |
| | 6.0 | 71.899<br>0.027 | 86.394<br>0.008 | 38.171<br>0.038 | 29.177<br>0.049 |

**Table 8**
Sensitivity of COFFA-GGVF to the threshold variation. Images in Figs. 10 and 11.

| Threshold/Series | $T_1-0.1T_1$; $T_2-0.1T_2$ | $T_1+0.1T_1$; $T_2-0.1T_2$ | $T_1-0.1T_1$; $T_2+0.1T_2$ | $T_1+0.1T_1$; $T_2+0.1T_2$ |
|---|---|---|---|---|
| Banana series | 86.891<br>0.005 | 82.704<br>0.010 | 87.351<br>0.005 | 81.911<br>0.010 |
| Plane series | 74.028<br>0.016 | 80.117<br>0.007 | 76.372<br>0.014 | 82.109<br>0.007 |
| E-series | 92.310<br>0.009 | 87.918<br>0.017 | 92.527<br>0.009 | 87.830<br>0.016 |
| Horseshoe series | 81.413<br>0.010 | 81.053<br>0.010 | 75.038<br>0.020 | 73.803<br>0.023 |
| Horseshoe series speckle noise | 86.136<br>0.005 | 85.930<br>0.004 | 79.164<br>0.007 | 77.391<br>0.004 |
| Synthetic tumor series, speckle noise | 96.423<br>0.004 | 92.014<br>0.008 | 96.813<br>0.004 | 91.711<br>0.009 |

the object whereas COFFA-GGVF still performs satisfactory. The required thresholds for COFFA-GGVF for this and all the forthcoming examples were obtained by the Otsu algorithm.

**Example 3.** Thirty noisy images.

This example shows the applicability of COFFA-GGVF to a variety of low contrast noisy images depicted in Fig. 10. Typical snake initializations are shown by points around the object. Images (a)–(d) are subjected to 2% Gaussian noise. Images (d) and (e) are subjected to a speckle noise characterized by variance $\sigma=2.0$ (see Fig. 10).

Note that since the images are characterized by a low contrast, the noise is not clearly visible. Therefore, images (f)–(i) represent the original images scaled to [0,1] to show that the impact of the noise is significant.

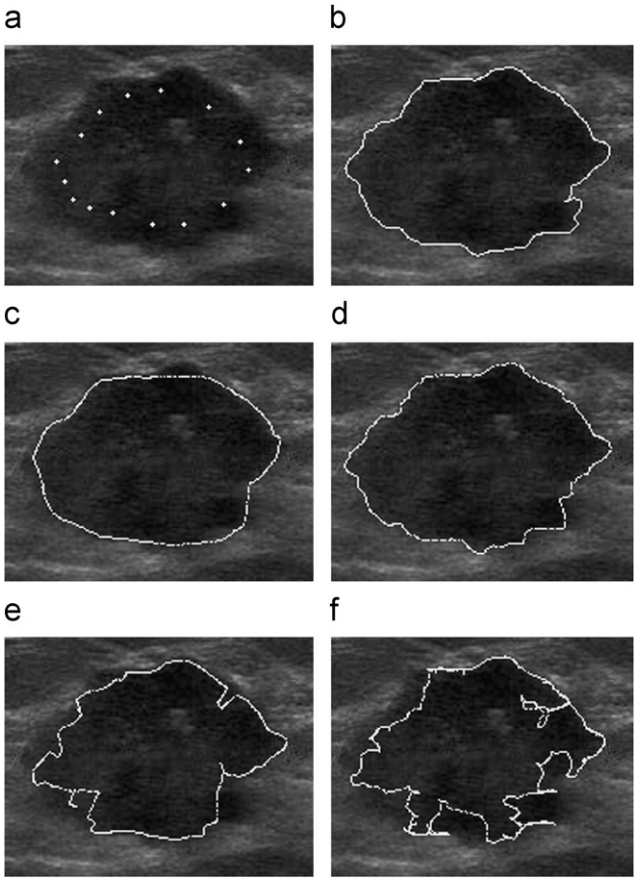


**Fig. 12.** Low contrast US image (a) ROI and a snake initialized inside the contour, (b) the ground truth, (c) GGVF, (d) COFFA-GGVF, $K=0.4$, (e) distance snake and (f) balloon snake.

Next, every image was distorted four times using the shear and the twirl transformations with different parameters creating a series of five test images (see Fig. 11).

Average accuracy and sensitivity tables are presented below. The method has been compared with GGVF, DS and the balloon snake (BS). Due to the noise, BS does not perform well and even diverged in several cases. The tables show that on average COFFA-GGVF is superior with regard to GGVF, DS and BS. Note that DS may work better when the threshold is selected manually (see Table 6 the Banana series) but still it cannot achieve the accuracy of COFFA-GGVF. Besides DS fails on the E-series since the snake gets attracted by another object as shown in Example 1. The plane series shows similar accuracy for GGVF, COFFA-GGVF and DS in terms of true positives. Both GGVF and COFFA-GGVF are 2 times better than DS in terms of the Hausdorff distance. However, COFFA-GGVF is an apparent winner for the E-series and the Horseshoe-series and the Tumor series with a 10–20% accuracy increase in terms of true positives and a clear advantage in terms of the Hausdorff distance.

Table 7 displays a better robustness of the new algorithm with reference to other methods. We also evaluated the sensitivity of the algorithm to thresholds $T_1$,$T_2$ selected by the Otsu algorithm. Table 8 shows the last experiment. Both thresholds have been varied by 10%, which constitutes a total of 20% change. However, even with this relatively large change the accuracy does not change significantly and is still appropriate (compare with Table 7, column COFFA-GGVF). Finally, note that the Otsu threshold is not optimal. Table 8 shows that there could be better thresholds obtained by a trail and error procedure. Nevertheless, Otsu's method provides an appropriate (but not the best) accuracy as applied for the COFFA-GGVF method.

## 6. Numerical experiments with ultrasound images of breast tumors

Detection of tumors in ultrasound (US) images by a trained physician is usually efficient and the number of false negatives is low. However, manual segmentation of the tumor boundary is

**Table 10**
The accuracy for different edge map methods. US image in Fig. 12.

| Method | GGVF | COFFA-GGVF | DS | BS |
|---|---|---|---|---|
| Prewitt | 55.900<br>0.032 | 79.785<br>0.012 | 34.806<br>0.052 | 45.935<br>0.061 |
| Sobel | 57.387<br>0.029 | 81.817<br>0.011 | 34.911<br>0.052 | 46.301<br>0.061 |
| Canny | 54.136<br>0.032 | 79.084<br>0.016 | 33.917<br>0.053 | 44.822<br>0.064 |

**Table 9**
Accuracy: GGVF, COFFA-GGVF, DS and BS vs. the ground truth. US image in Fig. 12; 110 iterations.

| Method/estimate | GGVF $K$ | | | COFFA-GGVF $K$ | | | DS $T=0.267$ | BS |
|---|---|---|---|---|---|---|---|---|
| | 0.01 | 0.1 | 0.4 | 0.01 | 0.1 | 0.4 | | |
| The best | 47.853<br>0.057 | 55.900<br>0.032 | 53.827<br>0.032 | 78.713<br>0.012 | 79.785<br>0.012 | 79.501<br>0.012 | 34.806 | 45.935 |
| The worst | 45.061<br>0.057 | 46.015<br>0.054 | 34.194<br>0.061 | 48.433<br>0.035 | 49.767<br>0.035 | 50.566<br>0.035 | 0.052 | 0.061 |
| Converg. | No | No | No | Yes | Yes | No | | |

**Table 11**
The accuracy for different initial contours. US image in Fig. 12.

| Distance (pixels) | GGVF | COFFA-GGVF | DS | BS |
|---|---|---|---|---|
| 3 | 70.401<br>0.024 | 81.612<br>0.012 | 38.037<br>0.029 | 54.282<br>0.055 |
| 6.8 | 55.900<br>0.032 | 79.785<br>0.012 | 34.806<br>0.052 | 45.935<br>0.061 |
| 8.4 | 53.219<br>0.054 | 73.471<br>0.014 | 32.102<br>0.057 | 25.315<br>0.071 |

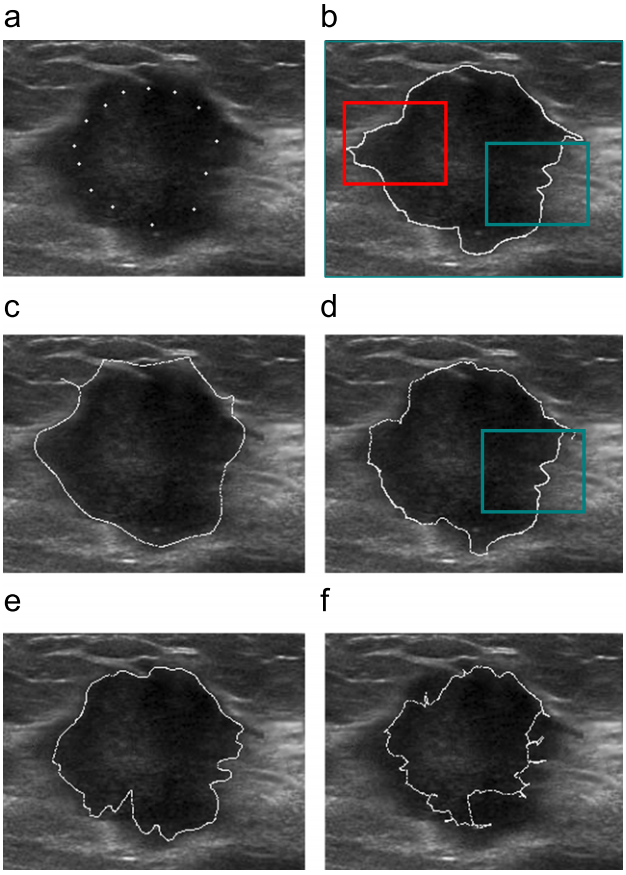


**Fig. 13.** Low contrast US image (a) ROI and a snake initialized inside the contour, (b) ground truth, (c) GGVF, (d) COFFA-GGVF, $K=0.4$, (e) DS and (f) BS.

tedious and time-consuming. Therefore, automatic segmentation techniques are important to help us to better visualize the tumor boundary, to calculate the volume of the tumor and to extract features needed for tumor classification (benign or malignant). The US images of the breast tumors are characterized by the low contrast, a high level of noise, speckles and tissue related textures obstructing the actual tumor. It is often the case that for these images the snake contour must be initialized very close to the object; otherwise it "does not feel" the edge of the actual object and converges to a false boundary. All the presented tumor images have been preprocessed using the density-weighted contrast enhancement filter [53] to better differentiate the background and tumor areas.

**Example 4.** A low contrast malignant tumor.

This example demonstrates the method applied to a low contrast US image of the breast tumor in Fig. 12(a). The ground truth image in Fig. 12(b) and the other ground truth images were outlined by Dr. Mavin Wongsaisuvan, who is currently a leading radiologist with the Queen Sirikit Center for Breast Cancer of King Chulalongkorn Memorial Hospital, Bangkok Thailand.

The results obtained with GGVF and COFFA-GGVF are shown in Fig. 12(c) and (d). They reveal that the conventional GGVF produces a smoother but less accurate contour as compared with the COFFA-GGVF. This conclusion is also supported by Table 9, which displays the accuracy for various diffusion coefficients.

Note that the maximum accuracy that has been achieved by GGVF with $K=0.1$ after 50 iterations is of 55.9% whereas COFFA-GGFV reaches 79.8% with 70 iterations and $K=0.1$. However, the iterations for GGVF diverge for every $K$. Therefore, even 55.9% is hardly achievable since it is not clear how to interrupt the iterations. The accuracy increase provided COFFA-GGVF with the reference to GGVF ranges between 17.6% and 54.9%. Finally, the DS and the BS perform extremely poor. This is because they

**Table 13**
The accuracy for different edge detection methods. US image in Fig. 13.

| Method | GGVF | COFFA-GGVF | DS | BS |
|---|---|---|---|---|
| Prewitt | 57.352<br>0.033 | 64.153<br>0.021 | 41.470<br>0.039 | 17.731<br>0.052 |
| Sobel | 55.961<br>0.033 | 66.081<br>0.020 | 42.151<br>0.034 | 17.782<br>0.052 |
| Canny | 53.180<br>0.034 | 64.102<br>0.023 | 40.390<br>0.036 | 16.081<br>0.051 |

**Table 12**
Accuracy: GGVF, COFFA-GGVF, DS and BS vs. the ground truth. US image in Fig. 13; 130 iterations.

| Iteration | GGVF $K$ | | | COFFA-GGVF $K$ | | | DS $T=0.239$ | BS |
|---|---|---|---|---|---|---|---|---|
| | 0.01 | 0.1 | 0.4 | 0.01 | 0.1 | 0.4 | | |
| The best | 38.507<br>0.043 | 56.327<br>0.033 | 57.352<br>0.033 | 63.766<br>0.026 | 64.153<br>0.021 | 61.378<br>0.030 | 41.470 | 17.731 |
| The worst | 35.437<br>0.046 | 38.180<br>0.043 | 9.247<br>0.051 | 58.393<br>0.033 | 59.346<br>0.031 | 52.956<br>0.031 | 0.039 | 0.052 |
| Converg. | No | No | No | Yes | Yes | Yes | | |

**Table 14**
The accuracy for different initial contours. US image in Fig. 13.

| Distance (pixels) | GGVF | COFFA-GGVF | DS | BS |
|---|---|---|---|---|
| 9.3 | 61.428<br>0.019 | 69.818<br>0.012 | 43.370<br>0.035 | 33.821<br>0.040 |
| 16.3 | 57.352<br>0.033 | 64.153<br>0.021 | 41.470<br>0.039 | 17.731<br>0.052 |
| 21 | 49.938<br>0.041 | 57.641<br>0.028 | 40.250<br>0.039 | 9.610<br>0.071 |

are easily attracted by small clusters of noise with a large amplitude. Finally, Tables 10 and 11 show the advantage of the proposed method with regard to the variety of underlying edge map methods and with regard to different initializations.

**Example 5.** A low contrast malignant tumor. Complicated shape. High noise.

Results similar to those from the previous example are obtained for a malignant tumor in Fig. 13(a). Table 12 reveals that COFFA-GGVF outperforms the standard GGVF at every iteration and for every diffusion coefficient.

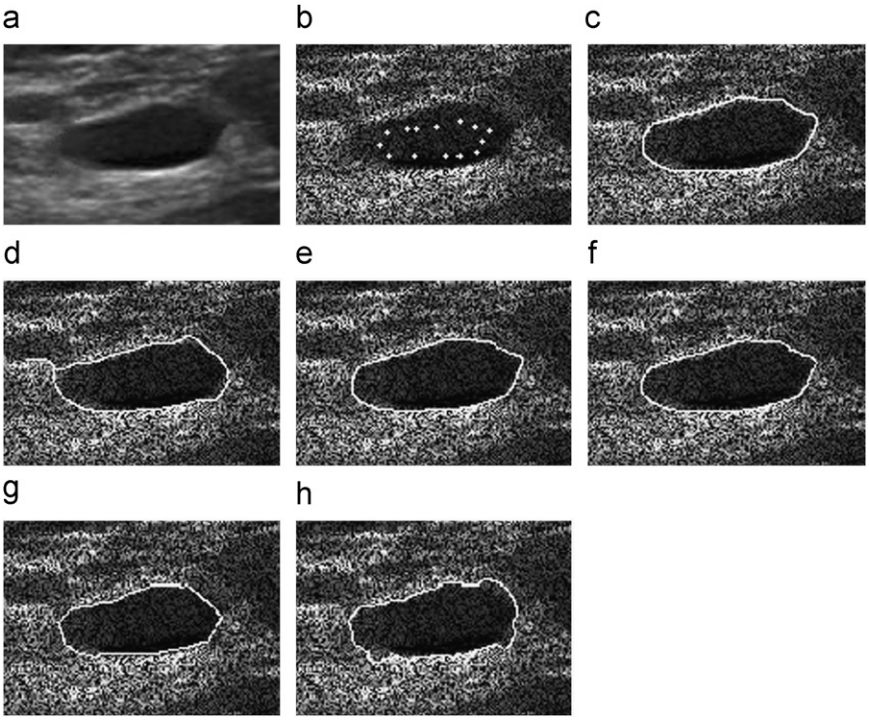


**Fig. 14.** (a) Original image (b) speckle noise $\sigma=0.4$ and a snake initialized inside the contour, (c) the ground truth, (d) GGVF, (e) COFFA-GGFF, (f) BS-COFFA-GGVF, $K=0.4$, (g) DS and (h) BS.

**Table 15**
Accuracy vs. the noise level: GGVF, COFFA-GGVF, DS, BS and BS-COFFA-GGVF. Image in Fig. 14.

| Speckle noise | | GGVF $K$ | | | COFFA-GGVF $K$ | | | DS | BS | BS-COFFA GGVF $K$ | | |
|---|---|---|---|---|---|---|---|---|---|---|---|---|
| | | 0.01 | 0.1 | 0.4 | 0.01 | 0.1 | 0.4 | | | 0.01 | 0.1 | 0.4 |
| 0.2 | The best | 42.42<br>0.027 | 80.52<br>0.011 | 84.64<br>0.010 | 98.33<br>0.003 | 98.82<br>0.003 | 98.59<br>0.004 | 75.61<br>0.018 | 67.15<br>0.013 | 98.62<br>0.003 | 98.71<br>0.003 | 98.13<br>0.003 |
| | The worst | 36.37<br>0.035 | 76.03<br>0.035 | 54.14<br>0.039 | 96.72<br>0.004 | 96.31<br>0.004 | 96.19<br>0.004 | $T=$<br>0.239 | | 96.04<br>0.003 | 96.40<br>0.004 | 96.68<br>0.003 |
| Converg. | | No | Yes | No | Yes | Yes | Yes | | | Yes | Yes | Yes |
| 0.4 | The best | 37.17<br>0.027 | 79.87<br>0.013 | 76.82<br>0.029 | 97.19<br>0.003 | 97.11<br>0.003 | 96.86<br>0.004 | 68.46<br>0.016 | 67.03<br>0.023 | 97.18<br>0.004 | 97.19<br>0.004 | 97.10<br>0.004 |
| | The worst | 21.70<br>0.029 | 62.39<br>0.041 | 62.38<br>0.046 | 76.72<br>0.035 | 77.20<br>0.035 | 76.76<br>0.034 | $T=0.241$ | | 78.04<br>0.032 | 76.10<br>0.031 | 77.26<br>0.031 |
| Converg. | | No | No | No | Yes | Yes | Yes | | | Yes | Yes | Yes |
| 0.6 | The best | 25.89<br>0.033 | 76.37<br>0.014 | 74.34<br>0.032 | 96.75<br>0.003 | 96.21<br>0.003 | 96.12<br>0.004 | 63.65<br>0.018 | 61.28<br>0.017 | 96.63<br>0.004 | 96.32<br>0.004 | 96.21<br>0.004 |
| | The worst | 25.05<br>0.037 | 55.45<br>0.036 | 48.40<br>0.030 | 74.59<br>0.038 | 75.10<br>0.038 | 72.79<br>0.044 | $T=$<br>0.247 | | 75.48<br>0.039 | 76.04<br>0.039 | 77.18<br>0.036 |
| Converg. | | No | No | No | Yes | Yes | Yes | | | Yes | Yes | Yes |

Fig. 13(c) and (d) demonstrates a typical difference between GGVF and COFFA-GGVF for large diffusion coefficients. The conventional GGVF creates such forces that certain segments of the snake collapse. This is because the free term of the GGVF equations over-smoothes the boundary. Eventually the boundary is "lost" and the snake collapses. As opposed to that COFFA-GGVF uses the adaptive edge map to calculate the gradient which is becoming smaller at the false boundaries and, therefore, does not over-smooth. The accuracy increase provided COFFA-GGVF with the reference to GGVF ranges from 40.0 to 80%. Note that GGVF diverges for $K=0.1$ and 0.4, whereas COFFA-GGVF remains stable although the accuracy is not good. Finally, note that only COFFA-GGVF resolves the strong edge outlined by the radiologist on the right side of the US image (Fig. 13(b) and (d)). However, all tested snakes failed to attach themselves to the corner-like boundary on the right side of the tumor (Fig. 13(a)).

The use of COFFA-GGVF and other methods with different edge maps is similar to the previous example (Table 10). The sensitivity shown in Tables 13 and 14 shows an advantage of the proposed scheme. Although on average the accuracy is low, the initial contour at a 9 point distance produces a reasonable accuracy of about 70% only when COFFA-GGVF is applied.

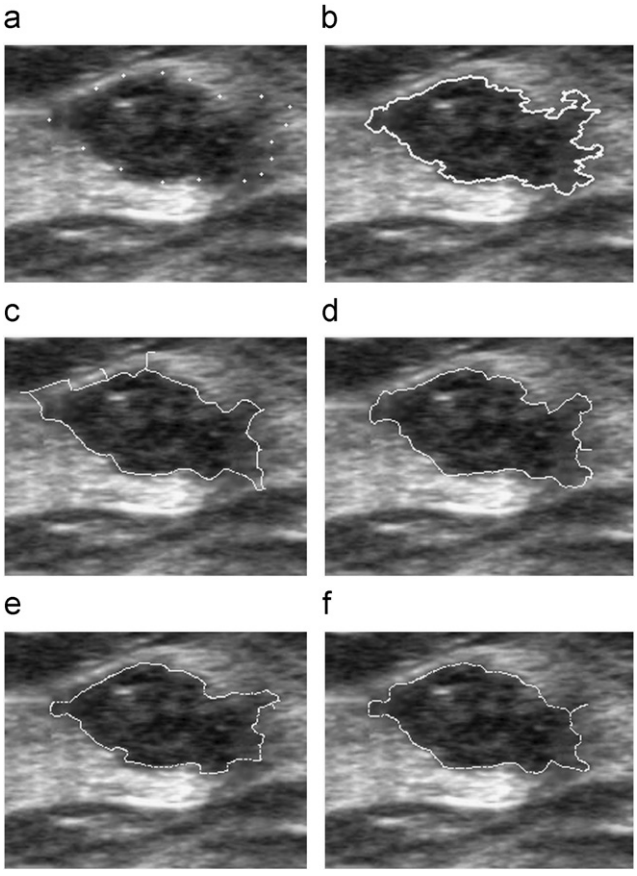


**Fig. 15.** Low contrast US image (a) ROI and a snake initialized outside the contour, (b) the ground truth, (c) GGVF, (d) COFFA-GGVF, $K=0.4$, (e) DS and (f) BS.

**Example 6.** A low contrast benign tumor. High noise.

This example demonstrates application of the proposed method to a relatively smooth benign tumor of the breast shown in Fig. 14(a).

We analyze GGVF, COFFA-GGVF, DS and BS. Besides a new combination BS–COFFA-GGVF has been tested. The image was subjected to an additional artificial speckle noise on top of the present natural noise (Table 15).

Although the conventional GGVF leads to higher smoothing, it does not work better even for the round shape. Only a small diffusion $K=0.1$ produces results comparable with COFFA-GGVF. Large diffusion coefficients destroy the boundary and collapse the snake.

DS and BS perform relatively good but still GGVF and COFFA-GGVF outperform these methods. Besides, DS required different thresholds for different levels of noise. Note that the original image itself is noisy; however, since the tumor is smooth and round it can be captured even with an additional speckle noise. Table 15 shows the best results produced by COFFA-GGVF vs. the other snakes subjected to an increasing level of noise.

Clearly, the conventional GGVF is more sensitive to the noise which produces a vector field characterized by repelling and attracting stars, which distract the snake from the actual boundary. Interestingly enough, the combination BS–COFFA-GGVF produced similar or even slightly better results for every tested level of noise. This shows that COFFA-GGVF can be successfully combined with other types of snakes.

**Example 7.** A low contrast malignant tumor. Complicated shape. High noise.

Finally consider a tumor with a very complicated shape outlined by a radiologist (Fig. 15(a) and (b)).

Fig. 15(c) and (b) displays the results obtained with GGVF and COFFA-GGVF. Clearly, the GGVF snake shows a lower accuracy and collapses at many points, whereas COFFA-GGVF collapses only once and provides a shape closer to the original. It is hard to expect a very high accuracy in the case of such a complex shaped tumor since the collapsed snake forms spikes shown in Fig. 15(c)–(f). Therefore, Table 16 displays accuracy in terms of the Hausdorff distance, which characterizes the spikes better than the true positives.

Clearly, COFFA-GGVF leads to a better accuracy. The best accuracy achieved for $K=0.1$ and $K=0.4$ is about 30% better than the best result obtained with GGVF. Finally, COFFA-GGVF converges, whereas the conventional GGVF diverges for *any K*.

## 7. Conclusions

The proposed adaptive edge map derived from continuous orientation force field analysis extends the generalized gradient vector flow method to the case of a nonlinear source term, which "remembers" the preceding iterations. The method provides an

**Table 16**
Accuracy: the Hausdorff distance. Image in Fig. 15.

| Method/estimate | GGVF $K$ | | | COFFA-GGVF $K$ | | | DS $T=0.231$ | BS $T=0.231$ |
|---|---|---|---|---|---|---|---|---|
| | 0.01 | 0.1 | 0.4 | 0.01 | 0.1 | 0.4 | | |
| The best | 0.014 | 0.012 | 0.012 | 0.008 | 0.008 | 0.009 | 0.014 | 0.017 |
| The worst | 0.014 | 0.013 | 0.015 | 0.013 | 0.013 | 0.014 | | |
| Converg. | No | No | No | Yes | Yes | Yes | | |

accuracy increase ranging from 10 to 80%, depending on the noise level, complexity of the contour and the accuracy measure, with the reference to the standard generalized gradient vector flow, the distance snake and the balloon snake. The model is less sensitive with regard to the distance between the initial contour and the object boundary. The method can be applied with a variety of edge detection methods and in many cases the required thresholds can be selected automatically using Otsu's algorithm. The method shows much promise as applied to detection of breast tumors in ultrasound images.

## Acknowledgement

This research is supported by Thailand Research Fund, grant BRG5380016.

We wish to thank the reviewers for valuable comments and suggestions.

## References

[1] M. Kass, A. Witkin, D. Terzopoulos, Snakes: active contour models, International Journal of Computer Vision 1 (4) (1988) 321–331.
[2] D.T. Kuan, A.A. Sawdhuck, T.C. Strand, P. Chavel, Adaptive restoration of image with speckle, IEEE Transactions on Acoustics, Speech and Signal Processing 35 (3) (1987) 373–383.
[3] A.N. Evans, M.S. Nixon, Biased motion-adaptive temporal filtering for speckle reduction in echocardiography, IEEE Transactions on Medical Imaging 15 (1) (1996) 39–50.
[4] F. Lefebvre, G. Berger, P. Laugier, Automatic detection of the boundary of the calcaneus from ultrasound parametric images using an active contour model; clinical assessment, IEEE Transactions on Medical Imaging 17 (1) (1998) 45–52.
[5] Y.S. Akgul, C. Kambhamettu, M. Stone, Extraction and tracking of the tongue surface from ultrasound image sequences, International IEEE Computer Society Conference on Computer Vision and Pattern Recognition, Santa Barbara, California (1998) 298–303.
[6] R. Chung, C.K. Ho, Using 2D active contour models for 3D reconstruction from serial sections, in: Proceedings of the 13th International IEEE Conference on Pattern Recognition, Vienna, Austria (1996) 849–853.
[7] A. Fenster, S. Tong, H.N. Cardinal, C. Blake, D.B. Downey, Three-dimensional ultrasound imaging system for prostate cancer diagnosis and treatment, IEEE Transactions on Instrumentation and Measurement 47 (6) (1998) 1439–1447.
[8] M.G. Strintzis, I. Kokkinidis, Maximum likelihood motion estimation in ultrasound image sequences, IEEE Signal Processing Letters 4 (6) (1997) 156–157.
[9] D.R. Chen, R.F. Chang, W.J. Wu, W.K. Moon, W.L. Wu, 3-D breast ultrasound segmentation using active contour model, Ultrasound in Medicine and Biology 29 (7) (2003) 1017–1026.
[10] R.F. Chang, W.J. Wu, W.K. Moon, W. Lee, D.R. Chen, Segmentation of breast tumor in three-dimensional ultrasound images using three-dimensional discrete active contour model, Ultrasound in Medicine and Biology 29 (11) (2003) 1571–1581.
[11] M. Cvancarova, F. Albresgtsen, K. Brabrand, E. Samset, Segmentation of ultrasound images of liver tumors applying snake algorithms and GVF, Congress Series 1281 (2005) 218–223.
[12] M. Aleman-Flores, P. Aleman-Flores, L. Alvarez-Leon, M.B. Esteban-Sanchez, R. Fuentes-Pavon, J.M. Santana-Montesdeoca, Computerized ultrasound characterization of breast tumors, International Congress Series 1281 (2005) 1063–1068.
[13] L.D. Cohen, On active contour models and balloon, CVGIP: Image Understanding 53 (2) (1991) 211–218.
[14] L.D. Cohen, I. Cohen, Finite-element methods for active contour models and balloons for 2-D and 3-D images, IEEE Transactions on Pattern Analysis and Machine Intelligence 15 (11) (1993) 1131–1147.
[15] T. McInerney, D. Terzopoulos, T-snakes: topology adaptive snakes, Medical Image Analysis 4 (2) (2000) 73–91.
[16] G. Giraldi, E. Strauss, A. Oliveira, Dual-T-Snakes model for medical imaging segmentation, Pattern Recognition Letters 24 (2003) 993–1003.
[17] H. Delingnette, J. Montagnat, New algorithm for controlling active contours shape and topology, Sixth European Conference on Computer Vision (ECCV), Ireland 2 (2000) 381–395.
[18] H. Delingette, J. Montagnat, Shape and topology constraints on parametric active contours, Computer Vision and Image Understanding 83 (2001) 140–171.
[19] B. Ostlad, A. Tonp, Encoding of a priori information in active contour models, IEEE Transactions in Pattern Analysis and Machine Intelligence 18 (9) (1996) 863–872.
[20] S.D. Fenster, J.R. Kender, Sectored snakes: evaluating learned energy segmentations, Transactions in Pattern Analysis and Machine Intelligence 23 (9) (2001) 1028–1034.
[21] M.-A. Charmi, S. Derrode, F. Ghorbel, Fourier-based geometric shape prior for snakes, Pattern Recognition Letters 29 (1) (2008) 897–904.
[22] C. Chesnaud, Ph. Réfrégier, V. Boulet, Statistical region snake-based segmentation adapted to different physical noise models, IEEE Transactions on Pattern Analysis and Machine Intelligence 21 (11) (1999) 1145–1157.
[23] R. Ronfard, Region-based strategies for active contour models, International Journal of Computer Vision 13 (2) (1994) 229–251.
[24] A. Chakraborty, L.H. Staib, J.S. Duncan, Deformable boundary finding in medical images by integrating gradient and region information, IEEE Transactions in Medical Imaging 15 (1996) 859–870.
[25] S.C. Zhu, A. Yuille, Region competition: unifying snakes, region growing, and Bayes/MDL for multiband image segmentation, IEEE Transactions in Pattern Analysis and Machine Intelligence 18 (9) (1996) 884–900.
[26] R. Malladi, J. Sethian, B. Vemuri, Shape modeling with front propagation, IEEE Transactions in Pattern Analysis and Machine Intelligence 17 (2) (1995) 158–171.
[27] S. Osher, J.A. Sethian, Fronts propagating with curvature dependent speed: algorithms based on Hamilton–Jacobi formulation, Journal of Computational Physics 79 (1988) 12–49.
[28] V. Caselles, R. Kimmel, G. Sapiro, Geodesic active contours, International Journal of Computer Vision 22 (1) (1997) 61–79.
[29] K. Siddiqi, Y.B. Lauzie're, A. Tannenbaum, S.W. Zucker, Area and length minimizing flows for shape segmentation, IEEE Transactions in Image Processing 7 (3) (1998) 433–443.
[30] X. Wang, L. He, W.G. Wee, Deformable contour method: a constrained optimization approach, International Journal of Computer Vision 59 (1) (2004) 87–108.
[31] L. He, Z. Peng, B. Everding, X. Wang, C.Y. Han, K.L. Weiss, W.G. Wee, A comparative study of deformable contour methods on medical image segmentation, Image and Vision Computing 26 (2008) 141–163.
[32] A. Yezzi, S. Kichenassamy, A. Kumar, P. Olver, A. Tannenbaum, Geometric snake model for segmentation of medical imagery, IEEE Transactions in Medical Imaging 16 (2) (1997) 199–209.
[33] F. Galland, N. Bertaux, Ph. Réfrégier, Minimum description length synthetic aperture radar image segmentation, IEEE Transactions on Image Processing 12 (9) (2003) 995–1006.
[34] M. Rochery, I.H. Jermyn, J. Zerubia, Higher order active contours, International Journal of Computer Vision 69 (1) (2006) 27–42.
[35] C. Xu, D. Pham, J. Prince, Image segmentation using deformable models, in: Handbook of Medical Imaging, vol. 2: Medical Image Processing and Analysis, SPIE Press, 2000, pp. 129–174.
[36] C. Li, J. Liu, M.D. Fox, Segmentation of external force field for automatic initialization and splitting of snakes, Pattern Recognition 38 (11) (2005) 1947–1960.
[37] C. Xu, J.L. Prince, Snakes, shapes, and gradient vector flow, IEEE Transaction on Image Processing 7 (3) (1998) 359–369.
[38] C. Xu, J.L. Prince, Gradient vector flow: a new external force for snakes, Proceedings of the International IEEE Computer Society Conference on Computer Vision and Pattern Recognition (1997) 66–71.
[39] C. Xu, J.L. Prince, Generalized gradient vector flow external forces for active contours, Signal Processing 71 (2) (1998) 131–139.
[40] J. Tang, A multi-direction GVF snake for the segmentation of skin cancer images, Pattern Recognition 42 (2009) 1172–1179.
[41] M. Wei, Y. Zhou, M. Wan, A fast snake model based on non-linear diffusion for medical image segmentation, Computerized Medical Imaging and Graphics 28 (3) (2004) 109–117.
[42] Z. Hou, C. Han, Force field analysis snake: an improved parametric active contour model, Pattern Recognition Letter 26 (2005) 513–526.
[43] J.M.S. Prewitt, Object enhancement and extraction, in: B.S. Lipkin, A. Rosenfeld (Eds.), Picture Processing and Psychopictorics, Academic Press, 1970.
[44] J.A. Canny, A computational approach to edge detection, IEEE Transaction in Pattern Analysis and Machine Intelligence 8 (1986) 679–714.
[45] I. Sobel, An isotropic $3 \times 3$ image gradient operator, in: H. Freeman (Ed.), Machine Vision for Three-Dimensional Scenes, Academic Press, 1990, pp. 376–379.
[46] C.F. Shu, R.C. Jain, Vector field analysis for oriented patterns, IEEE Transactions on Pattern Analysis and Machine Intelligence 16 (9) (1994) 946–950.
[47] W.Y. Yau, J. Li, H. Wang, Nonlinear phase portrait modeling of fingerprint orientation, IEE Control, Automation, Robotics and Vision Conference, December (2004) 1262–1267.
[48] J. Li, W.Y. Yau, H. Wang, Constrained nonlinear models of fingerprint orientations with prediction, Pattern Recognition 39 (1) (2006) 102–114.
[49] N. Otsu, A threshold selection method from gray-level histograms, IEEE Transactions on Systems Man and Cybernetics 9 (1979) 62–66.
[50] N. Hui-Fuang, Automatic thresholding for defect detection, Pattern Recognition Letters 27 (2006) 1644–1649.
[51] T. Lindeberg, Scale-Space Theory in Computer Vision, The Kluwer International Series in Engineering and Computer Science, Kluwer Academic Publishers, Dordrecht, Netherlands, 1994.
[52] R. Verdú-Monedero, J. Morales-Sánchez, L. Weruaga, Convergence analysis of active contours, Image and Vision Computing 26 (8) (2008) 1118–1128.
[53] N. Petrick, C. Heang-Ping, B. Sahiner, W. Datong, An adaptive density-weighted contrast enhancement filter for mammographic breast mass detection, IEEE Transactions on Medical Imaging 15 (1) (1996) 59–67.

**About the Author**—STANISLAV S. MAKHANOV recieved his M.Sc. in Applied Mathematics from the Moscow State University in 1981 and the Dr. Sc. from the Computing Center of the Russian Academy of Science in 1988, where he worked as Associate Professor until 1993.

From 1994 until 1999 he was a Visiting Professor with King Mongkut's Institute of Technology, Ladkrabang of Thailand and Associated Faculty with the Asian Institute of Technology.

He is currently Associate Professor with Sirindhorn International Institute of Technology, Thammasat University of Thailand. He is teaching courses in Applied Mathematics and Computer Science.

Dr. Makhanov has published about 100 research papers and conference proceedings on numerical methods and applications in robotics and image processing.

He has been a consultant to UN (ESCAP) and other international organizations.

Dr. Makhanov's biography has been published by Who is Who in the World 2005, Who is Who in Asia 2007 and Who's Who in Science and Engineering 2008 and 2010.